Successive Vapor-Phase Guerbet Condensation of Ethanol and 1-Butanol to 2-Ethyl-1-hexanol over Hydroxyapatite Catalysts in a Flow Reactor

Oksana V. Zikrata, Olga V. Larina,* Karina V. Valihura, Pavlo I. Kyriienko, Dmytro Yu. Balakin, Ivan Khalakhan, Katerina Veltruská, Andraž Krajnc, Gregor Mali, Sergiy O. Soloviev, and Svitlana M. Orlyk

Read Online

ACCESS | Metrics & More | Article Recommendations | Supporting Information

ABSTRACT: Calcium-containing hydroxyapatites including those modified with magnesium and strontium were prepared and tested as promising catalysts for the sustainable production of higher linear and branched alcohols from bioethanol. The hydroxyapatite catalysts were characterized by X-ray diffraction, scanning electron microscopy, energy-dispersive X-ray spectroscopy, X-ray photoelectron spectroscopy, Fourier transform infrared spectroscopy, and nuclear magnetic resonance spectroscopy, and temperature-programed desorption of NH_3 and CO_2. The partial replacement of Ca^{2+} ions by Mg^{2+} and Sr^{2+} in the hydroxyapatite structure was found to cause the deformation of its crystal lattice with the possible formation of amorphous calcium phosphate species. Moreover, there is both a decrease in the number and strength of the surface base sites of the catalysts and a redistribution of the strength of acid sites. The catalysts showed high activity and selectivity during the vapor-phase condensation of both aqueous ethanol into 1-butanol and 1-butanol into 2-ethyl-1-hexanol; however, a gradual deactivation of the catalysts occurs as a result of the blocking of aldol condensation sites. The highest selectivity values for 1-butanol and C_{4+} oxygenates (57 and 79.2% at 573 K and 0.36 $L \cdot L_{cat}^{-1} \cdot h^{-1}$) and for 2-ethyl-1-hexanol (77.5% at 573 K and 0.11 $L \cdot L_{cat}^{-1} \cdot h^{-1}$) were achieved over the calcium-containing hydroxyapatite catalyst modified with magnesium, which also showed an advanced resistance to deactivation with increasing time-on-stream.

KEYWORDS: *Guerbet condensation, ethanol and 1-butanol conversion, hydroxyapatite catalysts, Mg and Sr additives*
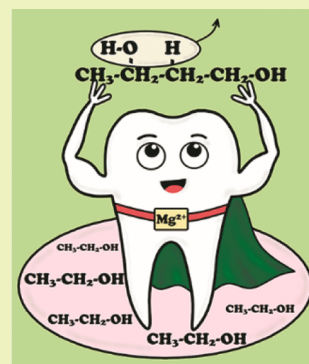
INTRODUCTION

The processes of synthesis of industrially important chemicals and fuels from the products of primary processing of renewable raw materials are a subject of sustainable chemistry research. In particular, bioethanol is used to produce many chemicals by catalytic conversion, and significant progress has already been made in obtaining a number of C_2-C_4 unsaturated hydrocarbons and oxygenates.[1−7] Also promising is the valorization of ethanol to obtain C_{6+} oxygenates and olefins, especially for the components of motor fuels.[8,9]

2-Ethyl-1-hexanol (2-EH) is generally used in the production of plasticizers, soaps, solvents, diesel additives, and other special chemicals.[10] The traditional production of 2-EH employs a technology of hydroformylation of propylene, self-condensation of butanal, and hydrogenation of 2-ethyl-2-hexenal.[11] An alternative one-step route consists of the synthesis of 2-EH through liquid-phase Guerbet coupling in a batch reactor with homogeneous−heterogeneous catalytic systems, that is, liquid base and solid noble metals; however, this process involves expensive separation, purification, recovery, and waste treatment sections.[12−14] Patel et al.[15] have proposed the concept of synthesis of 2-EH via successive

Guerbet condensation of ethanol (EtOH) and 1-butanol (BuOH) in a flow reactor (Scheme 1), being a cost-effective alternative to the traditional industrial method.

Despite the possibility of obtaining 2-EH in a flow reactor by an environment-friendly process from EtOH, there are a few works on this issue. Recently, 2-EH was synthesized from EtOH over $MgO-Al_2O_3$ catalysts for the first time.[16,17] Eagan et al.[18] have shown that the C_{4+} oxygenates produced by the Guerbet coupling of EtOH and BuOH can be easily converted into ethers with high cetane numbers. Given the high annual production amounts of 2-EH (3.3 million metric tons),[11] further targeted studies on obtaining 2-EH during vapor-phase ethanol catalytic conversion are required to address the sustainable manufacture of chemicals from bioethanol as a platform molecule.
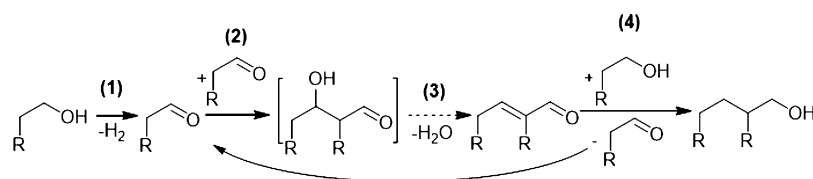
Scheme 1. Scheme of the Guerbet Reaction Mechanism: 1—Dehydrogenation of the Initial Alcohol to Aldehyde, 2—Aldol Condensation, 3—Dehydration of the Aldol Product to Unsaturated Aldehyde (Crotonic Condensation), 4—Hydrogenation and/or Reduction of Unsaturated Aldehyde according to Meerwein−Ponndorf−Verley

In the process of obtaining 1-butanol by vapor-phase condensation of ethanol, a wide range of catalysts have been investigated, including metal oxide systems, alkali cation zeolites, and hydroxyapatites (HAPs). Among others, HAP catalysts represent the most selective in EtOH-to-BuOH condensation.[14,19,20] The use of HAP additionally offers the possibility to tune the acid−base and redox surface properties by a modification of the stoichiometric form to the nonstoichiometric Ca-deficient system or the replacement of Ca^{2+} sites in calcium HAP (Ca-HAP) by other divalent and trivalent cations.[21]

Tsuchida et al.[22,23] and Wang et al.[24] have shown that the activity and selectivity of Ca-HAP in the EtOH-to-BuOH process strongly depends on the Ca/P ratio and the preparation method. Hanspal et al.[25] have shown that the Ca-HAP catalyst is more selective toward BuOH (72%) at an EtOH conversion of ∼5% in comparison with $Ca_3(PO_4)_2$ (35%) and $Sr_3(PO_4)_2$ (9%), while over $Mg_3(PO_4)_2$ BuOH did not form. The overall catalytic studies of EtOH-to-BuOH condensation over the aforementioned catalysts demonstrated the importance of Lewis acidity of the metal phosphates for the reaction. The relatively strong Lewis acid sites (LASs) of magnesium phosphate predominantly catalyzed EtOH dehydration, whereas in the case of strontium phosphate, the main product was acetaldehyde (AA).

Ogo et al.[26] have reported that higher BuOH selectivity in the EtOH-to-BuOH process was reached over Sr-HAP compared to Ca-HAP (81.5 and 75.3% at an EtOH conversion of ∼7%); however, Sr-HAP was characterized with lower productivity. It was also shown that with an increase in the Sr/P ratio from 1.58 to 1.70, EtOH conversion (from 1.1 to 11.3%) and BuOH selectivity (from 69.0 to 86.4%) rise thanks to the increasing surface density of the strong base sites O−Sr−O.[27] Silvester et al.[28] have shown that the ratio of concentrations of acid sites (C_a) and base sites (C_b) decreases with increasing Sr^{2+} content in CaSr-HAP systems. Thus, at the same EtOH conversion of 13%, the maximal BuOH selectivity (63.2%) is achieved over Sr-HAP at C_a/C_b = 4. Nevertheless, the performance of such catalysts is much lower compared to that of Ca-HAP.

Recently, Han et al.[29] have discovered that Ni/HAP allows the achievement of selectivity of 2-EH of 52.4% at BuOH conversion of 29.6% for Guerbet condensation using a high-pressure reactor. Also Wang et al.[30] have obtained 80.2% BuOH conversion and 79.1% 2-EH selectivity via a high-pressure reactor and Ni/Ca_xMg_yO catalyst. Tsuchida et al.[23] and Wang et al.[24] have registered the formation of C_{6+} Guerbet alcohols during ethanol conversion over Ca-HAP.

The transition from the use of absolute ethanol (100 vol %) to aqueous ethanol for the Guerbet process is another important research task to be waited to solve. The presence of H_2O in the ethanol feed has a significant effect on the

catalyst activity during the conversion in both autoclaves[31] and flow reactors.[32] Recently, the deposition of an active phase on a carbon carrier is shown to reduce the deactivating effect of H_2O on the indices of Guerbet condensation of ethanol over MgO[33] and $MgO−Al_2O_3$-containing catalyst.[34] However, the potential of using these catalysts for aqueous ethanol conversion remains unclear.

In view of the foregoing considerations, the key issue is the development of active and selective catalysts for obtaining 2-EH from bioethanol by the environment-friendly process of successive Guerbet condensation of EtOH-to-BuOH and BuOH-to-2-EH. Herein, we first investigate the effect of Ca-HAP modification by the partial substitution of Ca^{2+} ions by Mg^{2+} and Sr^{2+} in the HAP crystal structure as a possible way to increase the catalyst activity and selectivity during the mentioned processes. Rectified ethanol has been used as the feed. The partial substitution of Ca^{2+} by Mg^{2+} is found to increase the selectivity of 2-EH formation from 55 to 62%.

■ EXPERIMENTAL SECTION

Catalyst Preparation. Ca-containing HAP (Ca-HAP) with a Ca/P molar ratio of 1.67 was synthesized by the co-precipitation of calcium nitrate and diammonium hydrogen phosphate (pH = 11−12). 1 M solution of $(NH_4)_2HPO_4$ (120 mL) and 25% solution of NH_4OH (100 mL) were poured into a flask under stirring at room temperature (293 K). 1 M solution of $Ca(NO_3)_2·4H_2O$ (200 mL) was added dropwise to the mixture; then, 25% solution of NH_4OH (50 mL) and distilled water (100 mL) were added. For the synthesis of modified HAPs, 1 M solution of $Ca(NO_3)_2·4H_2O$ was mixed with a certain amount of 1 M solution of $Sr(NO_3)_2$ and $Mg(NO_3)_2·6H_2O$. Calcium (5 mol %) was replaced by strontium; in turn, 2.5 and 5 mol % calcium were replaced by magnesium. Further, the resulting mixtures were heated to 353 K and left to stir for 3.5 h. The suspensions were separated by hot filtration, washed with warm distilled water to neutral pH, and dried at 393 K for 2 h. The obtained HAPs were calcined at 873 K for 3 h and marked as CaSr5-HAP, CaMg2.5-HAP, and CaMg5-HAP.

Catalyst Characterization. The specific surface areas of the samples were evaluated by classical single-point BET surface area measurements on an apparatus of low-temperature nitrogen physisorption (GKh-1, USSR). Prior to the measurements, the samples were degassed at 673 K for 2 h under helium gas. Surface areas were determined by physical adsorption of N_2 at a liquid nitrogen temperature, using the BET equation.

The powdered X-ray diffraction (XRD) patterns of HAPs were recorded using a D8 Advance (Bruker AXS GmbH, Germany) diffractometer with Cu Kα radiation (nickel filter, λ = 0.154 nm).

The morphology of the samples was observed by means of scanning electron microscopy (SEM) using a Tescan MIRA 3 microscope (electron beam energy of 20 keV). The chemical composition mapping analysis was carried out using an energy-dispersive X-ray spectrometer equipped with a Bruker XFlash detector mounted directly onto the scanning electron microscope.

The surface composition of HAP catalysts was investigated using X-ray photoelectron spectroscopy (XPS) on an ultrahigh vacuum apparatus equipped with a SPECS Phoibos 150 hemispherical

analyzer using a conventional Al Kα source. The samples were fixed on a carbon tape. The Ca-HAP spectrum was recorded at 15 mA emission current, and the spectra of all other samples were recorded at 20 mA emission current. The XPS spectra were processed with the KolXPD software, subtracting the Shirley background and using Voigt profiles for fitting. The C 1s photoemission line was used for the binding energy calibration. To calculate the near-surface atomic ratios of Ca/P and (Ca + M)/P for the samples (M—Mg, Sr), Scofield sensitivity factors[35] and the areas of X-ray photoemission peaks from the Ca 2p, P 2p, Mg 2s, and Sr 3p core levels were used. The P 2s and Sr $3p_{3/2}$ photoemission lines were used to calculate the (Ca + Sr)/P ratio for the CaSr5-HAP sample, as the binding energies of P 2p and Sr 3d levels strongly overlap.

The Fourier transform infrared (FTIR) spectra of the HAP powders were recorded using a transmission mode on a PerkinElmer Spectrum One Fourier IR spectrometer with a spectral resolution of 2 cm^{-1}. A sample of 0.5 mg was dispersed in 44 mg of KBr and pressed at ~5 ton·cm^{-2} into thin wafers with a density of ~15 mg·cm^{-2}. The FTIR spectra were recorded at room temperature and atmospheric pressure in the wavenumber range of 4000−400 cm^{-1} with a resolution of 1 cm^{-1} and accumulating 120 scans.

The nature of the acid sites of the samples was studied by FTIR spectroscopy of adsorbed pyridine. Before adsorption/desorption experiments, the samples were pressed into thin wafers of ~10 mg·cm^{-2} and placed inside the FTIR cell. The wafers were outgassed under vacuum (1 Pa) at 698 K for 1.5 h. These wafers were exposed to gaseous pyridine at 423 K. The spectra were recorded after desorption at defined temperatures (423, 523, and 623 K) using a PerkinElmer Spectrum One Fourier IR spectrometer in the wavenumber range of 1650−1400 cm^{-1} with a resolution of 1 cm^{-1} and accumulating 24 scans.

The acid−base properties of the samples were studied by one-pass temperature-programed desorption (TPD) with mass spectrometry (MS) control: a chamber pressure of 10^{-7} Pa, a sample weight of 20 mg, a heating rate of 0.15 K/s, a short distance of 0.5 cm between the sample and the MS detector. A time-of-flight MSX-3PC (Electron, Ukraine) mass spectrometer with a sensitivity of 2.2 × 10^{-5} A·Torr^{-1} was used. Before the adsorption of NH$_3$ and CO$_2$ probe molecules, the samples were heated in a constant Ar flow (30 mL/min) at 873 K for 1 h and then cooled down to room temperature. Adsorption of NH$_3$ and CO$_2$ was performed using a gaseous solution of NH$_3$ and CO$_2$ in Ar (at a flow rate of 30 mL/min) for 12 h. The concentration of acid and base sites ($\mu mol·g^{-1}$) was identified from the amount of NH$_3$ and CO$_2$ adsorbed on the sample surface at a certain temperature. The desorption temperatures of NH$_3$ and CO$_2$ molecules were used to establish the strength of the acid and base sites on the sample surface.

^{31}P magic-angle spinning (MAS), ^{1}H MAS, and ^{1}H−^{13}C cross-polarization (CP)/MAS nuclear magnetic resonance (NMR) spectra were recorded on a 600 MHz Varian VNMRS spectrometer at a sample rotation frequency of 20 kHz. ^{31}P and ^{1}H MAS measurements were carried out using a 1.6 mm Varian CPMAS probe, whereas ^{1}H−^{13}C CPMAS measurements were performed with a 3.2 mm Varian CPMAS probe. Larmor frequencies for ^{31}P, ^{1}H, and ^{13}C nuclei were 242.63, 599.38, and 150.72 MHz, respectively. In the ^{1}H−^{13}C CP/MAS measurements, a CP scheme with a contact time of 5 ms and high-power proton decoupling was used; the repetition delay was 1 s and the number of scans was 72,000. ^{1}H MAS NMR experiments used a 90° pulse of 1.6 μs and a repetition delay of 80 s; the number of scans was eight. ^{31}P MAS NMR experiments employed a 90° excitation pulse of 1 μs and a repetition delay of 300 s; eight scans were collected for each spectrum. The chemical shift axes of ^{1}H and ^{13}C spectra were referenced to the corresponding signals of tetramethylsilane, and the chemical shift axis of ^{31}P spectra was referenced to the signal of the 85% solution of H$_3$PO$_4$.

Catalytic Activity Measurements. Catalytic activity tests were carried out in a fixed-bed flow quartz reactor with an inner diameter of 10 mm in the temperature range 573−673 K and under atmospheric pressure. Samples with grains of 0.25−0.5 mm were loaded into the reactor. Ethanol (95.6 vol %, H$_2$O is the rest) or 1-butanol (99.8 vol

%, H$_2$O is the rest) feed was introduced to the evaporator via a syringe infusion pump. Ar was used as the carrier gas with a flow of 10 mL·min^{-1}. Processes with ethanol were carried out at liquid hourly space velocities (LHSVs) of 0.12, 0.23, 0.35, 0.47, and 0.58 L·L$_{cat}^{-1}$·h^{-1}, and the corresponding EtOH gas hourly space velocities (GHSVs) were 47.5, 94.9, 142.4, 189.9, and 237.4 h^{-1}. For 1-butanol conversion, the LHSVs were 0.06, 0.11, 0.17, and 0.23 L·L$_{cat}^{-1}$·h^{-1} and GHSVs were 15, 30, 45.2, and 60.4 h^{-1}, respectively. Before the catalytic tests, the samples were annealed in Ar flow at 773 K for 1 h. The reagents and reaction products were fed through a thermostatic (433 K) gas line to a thermostatic (433 K) metering valve of a gas chromatograph (NeoCHROM, Ukraine) equipped with a FID detector and a capillary column HP-FFAP, 50 m × 0.32 mm. Ethylene, butene, 1,3-butadiene (BD), AA, acetone, 1-butanal, ethyl acetate, crotonaldehyde, diethyl ether (DEE), dibutyl ether (DBE), ethanol, 1-butanol, 1-hexanol, 2-ethyl-1-butanol, 2-EH, and 1-octanol were determined in accordance with the calibration gas solutions. The sampling of the reaction products (without using a cold trap for condensing liquids) allows taking into account other unidentified products with a certain error and saving the carbon balance (by C$_1$ moles).

The catalytic activity of the samples was characterized by alcohol conversion (X)

$$X_i = \frac{n_i^0 - n_i}{n_i^0} \cdot 100\%$$

where n_i^0 is the initial amount of C moles of alcohol (EtOH or BuOH) in the feed, and n_i is the amount of C moles of the unreacted alcohol in the stream of the reaction products.

Selectivity toward the products (S), yield (Y), and BuOH productivity (P) were calculated by the following formulas

$$S_j = \frac{n_j}{(n_i^0 - n_i)} \cdot 100\%$$

$$Y_j = \frac{X_i \cdot S_j}{100\%}$$

$$P_{BuOH} = \frac{Y_{BuOH} \cdot WHSV \cdot k}{100\%}$$

where n_j is the amount of C moles of identified carbon-containing product and k is the maximum possible amount of BuOH (0.804 g) that can be produced from 1 g of EtOH.

■ RESULTS AND DISCUSSION

Structural and Textural Properties. Powder diffracto-grams of the synthesized samples are shown in Figure 1 (detailed patterns with the designation of the planes are represented in Figure S1). All reflexes correspond to the crystal lattice of apatite (ICDD: 01-074-9780).[25] The introduction of Sr^{2+} and Mg^{2+} ions into the structure of HAP does not
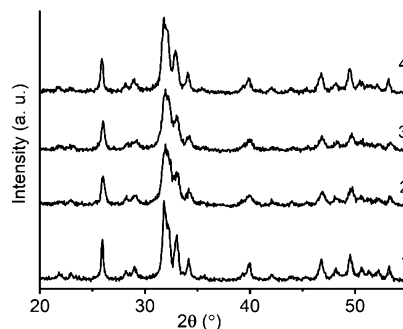

Figure 1. XRD patterns of the prepared samples: 1—Ca-HAP; 2—CaMg2.5-HAP; 3—CaMg5-HAP; and 4—CaSr5-HAP.

significantly affect the position of the peaks but leads to a certain decrease in their intensity. At the same time, for Sr-containing HAP, there is a slight shift of 0.2−0.3° to smaller angles of reflexes of the planes (1 1 2), (2 0 2), (3 0 1), and (4 0 2). This shift can be explained by the larger radius of Sr^{2+} ions (1.18 Å), which are embedded in the crystal lattice of HAP, compared to Ca^{2+} (1 Å).[36] The opposite effect is observed for magnesium, possibly due to the fact that the radius of Mg^{2+} ions (0.72 Å) is smaller than the radius of Ca^{2+}.[37] For the CaMg2.5-HAP sample, the reflexes at 29 and 49.5° correspond to the (2 1 0) and (2 1 3) planes, respectively. In turn, for the CaMg5-HAP sample, additional peaks at 28.2 and 45.3° are present, which correspond to the (1 0 2) and (2 0 3) planes, respectively. Therefore, we can conclude that the more substituted ions (Mg^{2+} and Sr^{2+}) present in the structure of calcium-containing HAP, the more strongly its crystal lattice is deformed.

The SEM micrographs of HAPs are depicted in Figure S2. The samples are characterized by a developed lamellar structure. The aggregates of unmodified Ca-containing HAP consist of elongated crystals 50−60 nm wide and up to 200 nm long. Tsuchida et al.[23] have noted that HAPs with a Ca/P ratio < 1.65 have a rodlike or lamellar structure, and with an increase in the ratio, particles become shorter. The replacement of both 2.5 mol % Ca by Mg and 5 mol % Ca by Sr in the composition of Ca-HAP leads to the formation of slightly smaller rod-shaped crystals of 25 to 60 × 95 to 120 nm. However, it is known[28] that the grain size of strontium-containing HAPs is larger than that without Sr. The introduction of 5 mol % Mg into the structure of HAP instead of Ca resulted in the formation of relatively large crystals of 60 to 80 × 150 to 230 nm.

Figure S3 shows the energy-dispersive X-ray spectroscopy (EDX) mapping of the distribution of P, O, Ca, Mg, and Sr elements on the surface of HAP calcined samples, indicating the homogeneity of the formed systems. The near-surface atomic ratios of Ca/P and (Ca + M)/P for the samples (M—Mg and Sr) are calculated according to XPS and are given in Table S1 (wide XPS scan of HAP samples is represented in Figure S4). The (Ca + M)/P ratio on the surface of CaMg2.5-HAP and CaSr5-HAP is almost intact (1.66−1.70) to the ratio for stoichiometric apatite (1.67). For unmodified HAP and CaMg5-HAP sample, the (Ca + M)/P ratio is slightly higher (1.72−1.76).

The infrared spectra of the synthesized HAP catalysts acquired in the range of 4000−400 cm^{-1} are represented in Figure 2. The absorption bands of phosphate and hydroxyl groups are present in all spectra, which are characteristic of HAPs. The bands at 606, 565, and 473 cm^{-1} can be attributed to the deformation asymmetric and symmetric oscillations. The bands at 1097, 1039, and 964 cm^{-1} can be assigned to the valence asymmetric and symmetric oscillations in PO_4^{3-}.[38] The stretching and libration modes of OH groups are observed at 3574 and 633 cm^{-1}, respectively.[39] The FTIR spectra show a strong decrease in the intensities of both bands of hydroxyl groups for Mg- and Sr-containing catalysts. The same tendency was observed for Sr-containing HAPs.[28] Wide bands in the range of 3670−3060 and 1720−1570 cm^{-1} refer to the valence and deformation oscillations of OH groups of water molecules, which are probably adsorbed on the surface of catalysts.[39] Additionally, there are bands in the range of 1470−1410 cm^{-1} and at 877 cm^{-1} assigned to the carbonate ions of type B (replacing phosphate groups).[40] CO_3^{2-} ions are present in
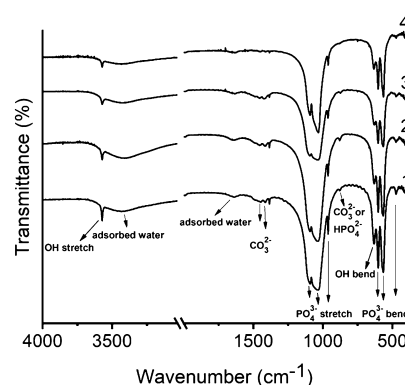
Figure 2. FTIR spectra of the synthesized samples: 1—Ca-HAP; 2—CaMg2.5-HAP; 3—CaMg5-HAP; and 4—CaSr5-HAP.

samples due to the adsorption of atmospheric CO_2.[39,41] However, the band at 877 cm^{-1} may also indicate the presence of HPO_4^{2-} groups.[42]

Figure S5 shows the ^{31}P and ^{1}H MAS NMR spectra of the synthesized HAPs. The spectra of all samples reveal the peaks at ~3.3 ppm, characteristic of the structural PO_4^{3-} groups of HAPs.[38,42−44] The ^{31}P MAS NMR spectra of CaMg2.5-HAP and CaMg5-HAP also show broad peaks centered at 5.3 ppm. The modification of HAP by Sr^{2+} ions is evidenced only by the shift of the maximum of the characteristic PO_4^{3-} peak to 3.4 ppm. Weak signals in the range from 13 to −3 ppm may indicate the presence of HPO_4^{2-} groups[42,43] belonging to certain defects of the crystal lattice. This is consistent with the FTIR spectra of the synthesized samples in Figure 2. The radius of Sr^{2+} (1.18 Å) is less different from Ca^{2+} (1 Å) than Mg^{2+} (0.72 Å), so probably the introduction of Sr^{2+} ions does not lead to a signal with high intensity in the discussed chemical shift range. The ^{1}H NMR spectra of all samples show signals at 0.1 and 5.3 ppm, characteristic of structural hydroxyl groups and structural/adsorbed water, respectively.[38,43,45] All spectra also show four additional peaks with some differences in specific positions. The spectra exhibit a peak with a maximum in the range from 0.9 ppm for CaMg5-HAP to 1.3 ppm for CaSr5-HAP, which is attributed to the structured water molecules on the surface of HAPs.[43] Peaks with maxima at 1.9−2.5 and 3.5−4 ppm might be assigned to either OH groups or isolated water molecules, as there are no hydrogen atoms attached to the aliphatic carbon atoms in the samples. Ben Osman et al.[43] attribute the signals in the last range (3.5−4 ppm) to structural HPO_4^{2-} groups. Signals in the range of 5.8−7.5 ppm might be attributed to acidic P−OH moieties associated with amorphous calcium phosphate species.[46]

The formation of the HAP structure in the synthesized samples was confirmed by XRD, FTIR, and NMR spectroscopy. At the same time, the introduction of Mg^{2+} or Sr^{2+} ions into the structure of Ca-HAP causes the deformation of its crystal lattice and the formation of amorphous calcium phosphate species. According to SEM and EDX, the samples are characterized by a developed homogeneous lamellar structure.

Acid−Base Properties. The acid−base characteristics of HAP samples were investigated by TPD of the probe molecules NH_3 and CO_2 and by FTIR spectroscopy of adsorbed pyridine.

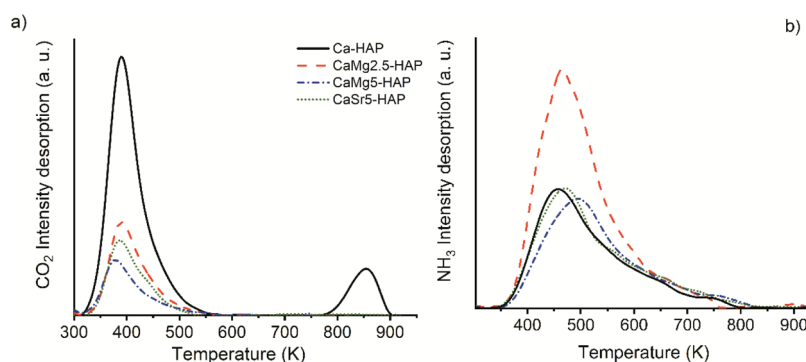TPD-CO_2 profiles are shown in Figure 3 and the deconvoluted spectra are shown in Figure S6. On the TPD-

Figure 3. TPD-CO_2 (a) and TPD-NH_3 (b) profiles of the HAP samples.

Table 1. Acid−Base Characteristics of the HAP Samples Calculated from TPD-NH_3 and TPD-CO_2

Ca-HAP (S_{BET} = 29 m²/g)		CaMg2.5-HAP (S_{BET} = 35 m²/g)		CaMg5-HAP (S_{BET} = 28 m²/g)		CaSr5-HAP (S_{BET} = 45 m²/g)	
T_{max},[a] K	C, μmol/g [μmol/m²]	Tmax, K	C, μmol/g [μmol/m²]	Tmax, K	C, μmol/g [μmol/m²]	Tmax, K	C, μmol/g [μmol/m²]
Basicity							
388	51 [1.76]	388	16 [0.46]	379	10 [0.36]	384	11 [0.24]
431	33 [1.14]	428	16 [0.46]	427	9 [0.32]	421	17 [0.38]
850	13 [0.45]						
total	**97 [3.35]**		**32 [0.92]**		**19 [0.68]**		**28 [0.62]**

Ca-HAP (S_{BET} = 29 m²/g)		CaMg2.5-HAP (S_{BET} = 35 m²/g)		CaMg5-HAP (S_{BET} = 28 m²/g)		CaSr5-HAP (S_{BET} = 45 m²/g)	
T_{max},[a] K	C, μmol/g [μmol/m²]	T_{max}, K	C, μmol/g [μmol/m²]	T_{max}, K	C, μmol/g [μmol/m²]	T_{max}, K	C, μmol/g [μmol/m²]
Acidity							
		412	12 [0.34]	424	17 [0.61]		
446	66 [2.28]	459	120 [3.43]	489	75 [2.68]	466	106 [2.36]
523	66 [2.28]	515	97 [2.77]	581	48 [1.71]	570	21 [0.47]
635	16 [0.55]	631	37 [1.06]	686	8 [0.29]	646	23 [0.51]
730	8 [0.28]			764	7 [0.25]	741	5 [0.11]
total	**156 [5.39]**		**266 [7.60]**		**155 [5.54]**		**155 [3.45]**

[a]Temperature maximum of peak desorption.

CO_2 profiles of all samples, the asymmetric peaks with maxima at temperatures of ∼385 K and expansion into a higher temperature region are observed, which indicate the presence of weak and medium base sites on the sample surface. The TPD-CO_2 profile of Ca-HAP also reveals a peak with a maximum at 850 K attributed to the strong base sites. Mg- and Sr-containing HAPs are characterized by a lower content of weak and medium base sites, as well as by the absence of strong base sites (Table 1). Thus, according to the change in the total concentration of the base sites, the synthesized samples are arranged in the following sequence: Ca-HAP 97 μmol·g^{-1} > CaMg2.5-HAP 32 μmol·g^{-1} > CaSr5-HAP 28 μmol·g^{-1} > CaMg5-HAP 19 μmol·g^{-1}. The total density of the base sites on the surface varies from 3.35 to 0.62 μmol·m^{-2} in the sequence: Ca-HAP > CaMg2.5-HAP > CaMg5-HAP > CaSr5-HAP.

In Figure 3b the TPD-NH_3 profiles have the asymmetric peak with a maximum in the temperature range of 459−489 K, which can be attributed to the superposition of ammonia desorption from weak and medium strength acid sites. The results of deconvolution of TPD-NH_3 spectra are shown in Figure S7. The shoulder in the range of 583−783 K can be attributed to the strong acid sites. The CaMg2.5-HAP sample is characterized by a significantly higher concentration of acid sites of 266 μmol·g^{-1} compared to the Ca-HAP sample with 156 μmol·g^{-1}. In the case of CaMg5-HAP and CaSr5-HAP, the total concentration of acid sites for both samples is similar, 155

μmol·g^{-1}. There is some redistribution of acid sites observed in terms of strength without changing their total content, contrary to Ca-HAP. Meanwhile, the total density of surface acid sites for Ca-HAP, CaMg5-HAP, and CaSr5-HAP differs significantly (5.39, 5.54, and 3.45 μmol·m^{-2}, respectively).

The comparison of acid−base characteristics with Ca/P and (Ca + M)/P ratios on the surface of the studied samples (Table S1) indicates that the increase in the concentration of base sites on the surface of Ca-HAP is caused by the excess of calcium cations in the sample. The ratio of Ca/P = 1.72 is higher than that in stoichiometric apatite (1.67). For samples modified with magnesium, the Ca/P ratio is less than 1.67, that is, the samples are characterized by a lower concentration of base sites and a higher concentration of acid sites, which is consistent with the results of Tsuchida et al.[23] Given that the (Ca + Mg)/P and Ca/P ratios are close and the surface concentration of the base sites in Mg-containing samples is smaller, we can assume that the surface OH groups are strong base sites.[47] The content of 2.5% Mg in calcium HAP contributes to a significant increase in acidity, which may be due to an increase in the structural defects of Mg-containing HAPs. It is consistent with the results of XRD, NMR, and FTIR spectroscopy. The increase in the structural defects of HAP can also explain the increase in the specific surface area of CaMg2.5-HAP by ∼20%. However, the increase in the magnesium content to 5% does not lead to increase in both total acidity and specific surface area, while the strength and

density of acid sites on the surface increase slightly. It could be explained by a significant excess of magnesium ions on the surface, $(Ca + Mg)/P = 1.76$, and partial blocking of the acid sites.

It should be noted that the high value of $(Ca + M)/P$ does not indicate the formation of strong base sites on the surface. For CaSr5-HAP, the ratio of $(Ca + Sr)/P$ is close to the value of stoichiometric apatite, but the concentration of the base sites is lower than that of Ca-HAP and CaMg2.5-HAP and is quite similar with the Ca-HAP concentration of acid sites. Moreover, the specific surface area of CaSr5-HAP is much larger than that of Ca-HAP, although the defects of the HAP structure is not observed by XRD, NMR, and FTIR spectroscopy; as a consequence, the specific values of acidity and basicity for CaSr5-HAP are not increased compared to Ca-HAP. According to Silvester et al.,[28] despite the higher basicity of strontium, the substitution of Ca^{2+} with Sr^{2+} does not always lead to an increase in the number or strength of the base sites of HAP. In the structure of HAP, calcium atoms coordinate with nine $Ca(1)$ and seven $Ca(2)$ oxygen atoms. The higher coordination number of calcium atoms provides stronger base sites formed with its participation. That is, samples in which Sr^{2+} cations replace $Ca(1)$-containing positions will have stronger base sites compared to samples with replaced $Ca(2)$ positions. The replacement of calcium by strontium in HAP is uneven, so there is an irregular change in basicity in strontium-containing systems. A similar situation may occur in the case of replacement of Ca^{2+} by Mg^{2+}, as indicated by the difference in the acid−base characteristics of CaMg2.5-HAP and CaMg5-HAP samples. Due to the smaller radius of Mg^{2+} ion (0.72 Å),[37] compared to Ca^{2+} (1 Å),[36] it can more easily replace the $Ca(1)$-containing positions of the HAP structure. The total concentration of the base sites of Mg-containing HAPs is likely to decrease due to the disappearance of strong $Ca(1)$-containing base sites and formation of the corresponding weaker Mg-containing base sites. Herewith, the total acidity of Mg-containing HAPs rises due to the formation of acid sites by Mg^{2+} cations on the surface.

The FTIR spectra of adsorbed pyridine over HAP samples are shown in Figure 4. For all samples, there are absorption bands at 1600 and 1575 cm^{-1}. The bands at 1600 and 1445 cm^{-1} are the most intensive for CaSr5-HAP and least intensive for CaMg5-HAP. They can be attributed to the coordination interaction of pyridine with LAS. However, on the FTIR spectra of Mg-containing HAPs, there are bands at 1607 and

$\sim$1455 cm^{-1}, which probably refer to the oscillations caused by the interaction of pyridine with Mg-containing LAS. Due to the superposition of oscillations of carbonate ions in the range of 1470−1410 cm^{-1}, it is difficult to estimate the acid characteristics of the samples by the absorption band intensity. The presence of the band at 1575 cm^{-1} in the FTIR spectra can be explained by the physical adsorption of pyridine on the surface of the samples.

Hence, the partial replacement of Ca^{2+} cations by Mg^{2+} or Sr^{2+} in the Ca-HAP structure leads to a decrease in the number and strength of base sites on the sample surface and the redistribution of acid sites. For the CaMg2.5-HAP sample, a significant increase in the number of acid sites was revealed.

Catalytic Properties. The results of the catalytic tests of HAP samples in EtOH gas-phase condensation processes under identical conditions are given in Tables 2 and S2. The highest values of EtOH conversion and yields of BuOH and C_{4+} oxygenates are achieved in the presence of Ca-HAP and CaMg2.5-HAP. C_{4+} oxygenates include BuOH, products of subsequent condensation of BuOH with EtOH, and self-condensation of BuOH. The conversion of ethanol and the yield of EtOH condensation products on the CaMg5-HAP catalyst are slightly lower. In the presence of CaSr5-HAP, EtOH conversion is twice lower, and the yield of BuOH and C_{4+} oxygenates is 3 times lower than those over Ca-HAP and CaMg2.5HAP.

In the presence of the Ca-HAP catalyst, in addition to EtOH condensation products, AA, ethylene, DEE, and small amounts of acetone, ethyl acetate, and crotonaldehyde were identified. Butenes and DBE were not detected, but small amounts of 1-butanol, an intermediate of the EtOH-to-BuOH and BuOH-to-2-EH transformations, were found. In the presence of Mg- and Sr-modified HAP catalysts, in particular CaSr5-HAP, the yield of the byproducts of ethanol dehydration (ethylene + DEE) and BD is higher, which may be caused by the formation of additional Mg- and Sr-containing LAS on the surface, compared to Ca-HAP.

As can be seen from Table 2, the yield of BuOH and C_{4+} oxygenates decreases with increasing time-on-stream (TOS) over the catalysts. The results of the stability study for the most active modified catalyst, that is, CaMg2.5-HAP, are shown in Figure S8. Over 20 h, the conversion of EtOH in the presence of CaMg2.5-HAP gradually decreases from 46.6 to 8.6%, with the largest decrease observed during the first 3 h. The BuOH selectivity decreases from 55 to 20.6%, which leads to a decrease in the yield of BuOH and C_{4+} oxygenates. At the same time, with the increase of TOS, the selectivities of BD and ethylene + DEE formation gradually increase. In turn, the AA selectivity increases significantly from 1.8 to 50.4%, indicating that the process is limited by the AA condensation step, which is typical of the vapor-phase Guerbet process in a flow reactor.[48]

A heterogeneous catalyst deactivation is commonly observed during the aldol condensation of AA, and it is most likely to be a result of the formation of high-molecular-weight compounds during the sequential conversion reactions of the obtained aldehyde.[32,49−51] This is also confirmed by ^{1}H and ^{13}C NMR spectroscopy for HAP catalysts after the reaction (see Figure S9). Moreover, water released in the Guerbet reaction and EtOH dehydration can also block the aldol condensation sites.[31,52,53] As we have recently shown, at a temperature of 573 K, the formation and adsorption of H_2O on the surface of the Guerbet condensation catalyst is the main reason for the
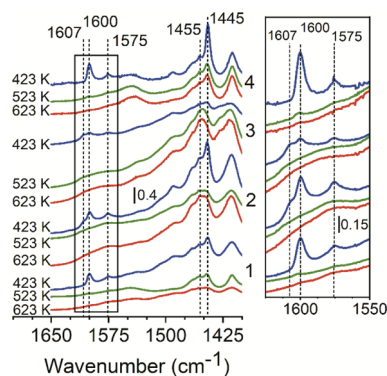

Figure 4. FTIR spectra of adsorbed pyridine on the synthesized HAPs: 1—Ca-HAP; 2—CaMg2.5-HAP; 3—CaMg5-HAP; and 4—CaSr5-HAP.

Table 2. Indices of Ethanol Conversion over the HAP Catalysts (T = 573 K, LHSV = 0.12 $L \cdot L_{cat}^{-1}$ h^{-1})

| catalyst | TOS, h | conv., % | yield, % | | | | | | |
			C_{4+} oxygenates	BuOH	1-butanal	BD	AA	ethylene + DEE	others
Ca-HAP	1.5	32.1	26.7	17.3	0.2	0.5	0.6	0.4	3.7
	2.5	22.6	18.6	13.1	0.1	0.4	0.7	0.3	2.4
	4	15.4	11.6	8.8	0.1	0.5	0.9	0.4	1.8
CaMg2.5-HAP	1.5	35.6	27.1	17.4	0.5	0.8	1.5	0.5	5.1
	2.5	19.4	13.6	10.1	0.4	0.4	2.0	0.4	2.6
	4	20.3	12.5	9.6	0.6	0.6	2.9	0.5	3.0
CaMg5-HAP	1.5	22.7	16.0	12.0	0.2	1.0	1.1	0.5	4.1
	2.5	17.8	11.9	9.4	0.1	1.0	1.2	0.5	3.0
	4	13.9	8.5	7.1	0.1	1.0	1.3	0.5	2.5
CaSr5-HAP	1.5	16.8	8.1	5.9	0.1	3.4	0.9	1.3	3.0
	2.5	10.0	3.9	2.6	0.0	2.4	1.0	1.2	1.5
	4	6.8	1.7	1.4	0.0	1.9	1.0	1.1	1.0

Table 3. Initial Product Selectivities in the EtOH-to-BuOH Process over the HAP Catalysts at T = 573 K

| catalyst | LHSV, $L \cdot L_{cat}{-1}$ $h{-1}$ | conversion, % | selectivity, % | | | | | | |
			C_{4+} oxygenates	BuOH	BD	1-butanal	AA	ethylene + DEE	others
Ca-HAP	0.31	23.1	83.2	56.2	1.0	0.5	3.4	0.9	11.1
CaMg2.5-HAP	0.36	20.4	79.2	57.0	1.5	0.7	3.4	1.0	12.9
CaMg5-HAP	0.37	20.2	72.5	54.7	2.4	0.6	5.7	1.5	17.3
CaSr5-HAP	0.12	18.2	57.7	46.2	13.9	0.4	4.0	5.4	18.7

Table 4. Indices of BuOH Conversion over the HAP Catalysts (T = 573 K, LHSV = 0.11 $L \cdot L_{cat}^{-1} \cdot h^{-1}$)

| catalyst | TOS, h | conversion, % | yield, % | | | | |
			2-EH	1-butanal	DBE	butenes	others
Ca-HAP	1.5	48.1	38.0	1.1	0.1	1.0	7.8
	2.5	38.2	29.1	1.3	0.2	1.0	6.6
	4	28.0	20.5	1.5	0.2	1.0	4.9
CaMg2.5-HAP	1.5	34.3	25.9	1.7	0.1	0.4	6.2
	2.5	36.1	28.0	1.6	0.1	0.4	6.0
	4	30.7	22.3	1.7	0.1	0.5	6.1
CaMg5-HAP	1.5	20.9	12.3	1.7	0.3	0.7	6.0
	2.5	19.3	11.9	1.6	0.3	0.6	4.9
	4	14.1	6.9	1.9	0.3	0.7	4.3
CaSr5-HAP	1.5	12.8	4.4	1.7	0.3	1.7	4.8
	2.5	9.4	2.3	1.8	0.3	1.7	3.3
	4	7.2	1.0	2.0	0.3	1.8	2.1

decrease in activity with TOS increasing.[34] Nevertheless, the deactivation of the HAP catalyst is reversible, and both the activity and selectivity of the catalyst under study can be fully reproduced after its regeneration at 773 K in the airflow for 1 h.

Initial selectivity in the EtOH-to-BuOH process over the HAP catalysts was compared at the same conversion of ~20%, achieved by the changing of LHSV, in Table 3. The highest selectivity for BuOH and C_{4+} oxygenates is achieved in the presence of Ca-HAP (56.2 and 83.2%) and CaMg2.5-HAP (57.0 and 79.2%). At the same time, selectivities toward other products over Ca-HAP and CaMg2.5-HAP are similar. In the case of CaMg5-HAP, the selectivities of BuOH and C_{4+} oxygenate formation are slightly lower (54.7 and 72.5%), while the selectivities of BD and AA are higher. The CaSr5-HAP sample is characterized by the lowest selectivity for BuOH and C_{4+} oxygenates among the investigated HAPs, yet the values of the selectivity of BD and ethylene + DEE are several times higher. This may be attributed to the greater

number of weak LAS on the sample surface, according to the FTIR spectra in Figure 4.

Figure S10 depicts EtOH conversion, BuOH yield, and selectivity toward the main products over CaMg2.5-HAP depending on temperature using fixed LHSV = 0.12 $L \cdot L_{cat}^{-1}$. As the temperature increases from 573 to 673 K, the EtOH conversion values increase from 19.4 to 92%, while the selectivity for BuOH and C_{4+} oxygenates decreases rapidly. In turn, the selectivity toward EtOH dehydration products (from 2 to 14%) and other EtOH condensation products, in particular olefins and BD (from 2 to 20.3%), increases, which corresponds to the thermodynamic process.[54] It is also in agreement with the results of calculations of the equilibrium composition of EtOH conversion products (BD and BuOH) in the 400−800 K temperature range. At temperatures above 550 K, BD is thermodynamically more favorable to form than BuOH.[55] In addition, higher temperatures are favorable for the dehydrogenation of BuOH to 1-butanal[14] and its subsequent conversion to C_{5+} products. The highest BuOH yield of 17.8%

at fixed LHSV is achieved in the presence of CaMg2.5-HAP at 598 K.

With an increase in LHSV from 0.12 to 0.58 $L \cdot L_{cat}^{-1} h^{-1}$, the conversion of EtOH decreases from 93.5 to 54.8% in the presence of CaMg2.5-HAP, but the selectivity and yield of BuOH increase from 2.8 to 28.9% and from 2.7 to 15.9%, respectively (Figure S11). Although the selectivity and yield of C_{4+} oxygenates increase, the BD selectivity decreases markedly from 19.9 to 14.6%. This may indicate different rates of BD and 1-butanol formation on HAPs. At the same time, the selectivity for ethylene + DEE decreases from 15.4 to 9.8%, while the AA selectivity remains almost intact (6−8%), that is, with the increase of LHSV, the ethanol dehydrogenation outspeeds the dehydration. A significant increase in the BuOH productivity of the catalyst CaMg2.5-HAP can be achieved at a higher process temperature (673 K) and LHSV (Figure S11b).

Indices of the gas-phase condensation of BuOH into 2-EH over HAP catalysts at the same conditions are given in Tables 4 and S3. The highest BuOH conversion and 2-EH yield achieved in the presence of Ca-HAP and CaMg2.5-HAP is similar to the EtOH-to-BuOH process. Over the CaMg5-HAP catalyst, the conversion of 1-butanol and the yield of 2-EH are decreased almost twice. The BuOH conversion and the yield of the target product over CaSr5-HAP are even lower in comparison with previous catalysts. Instead, the yield of byproducts, especially of BuOH dehydration, is much higher. The same trend was revealed in EtOH conversion. The analysis of the obtained data indicates the lower activity of strontium-modified HAP compared to Ca- and Mg-containing samples in the conversion of 1-butanol into 2-EH.

With the increase of TOS (Figure 5), the BuOH conversion and 2-EH selectivity over Ca-HAP and CaMg2.5-HAP catalysts decrease. During the first 5 h of catalytic reaction, the conversion of BuOH over Ca-HAP decreases significantly from 50.4 to 26.2%, while the selectivity of 2-EH remains at the same level of 72−79%. After 20 h of operation, the conversion of BuOH and selectivity of 2-EH are significantly reduced up to 5.8 and 20%, respectively. In turn, the selectivity toward butenes, DBE, and 1-butanal increases. This can be explained by the gradual deactivation of the catalysts as a result of blocking of the aldol condensation sites. Probably, the $[CaO]/[PO_4]^{3-}$ acid−base pairs are the active sites for 1-butanal condensation, as well as for the AA condensation reaction.[56] In the presence of CaMg2.5-HAP, BuOH conversion changes from 30 to 24% during the first 5 h of operation and then decreases to 8.6% after 20 h. The selectivity of the 2-EH formation of 67% is stable for the first 5 h and decreases after 20 h to 35.4%. The selectivities toward other products increase slightly: butenes up to 6% and 1-butanal up to 26%. The analysis of 1-butanal and 2-EH yields indicates that 1-butanal condensation sites are deactivated faster than the 1-butanol dehydrogenation sites. Deactivation of the catalysts with increasing TOS during the BuOH-to-2-EH process is a result of the formation of high-molecular-weight compounds during sequential conversion reactions of the obtained aldehyde, which is confirmed by the results of $^1H-^{13}C$ CP/MAS and ^1H MAS NMR (see Figure S9).

In the process of BuOH conversion, the CaMg2.5-HAP catalyst showed an advanced resistance to deactivation. The reaction of aldol condensation of butanal may occur over both the acid and base surface sites.[57] Given the acid−base characteristics of the samples, there are predominantly base sites on the surface of Ca-HAP, while on the surface of
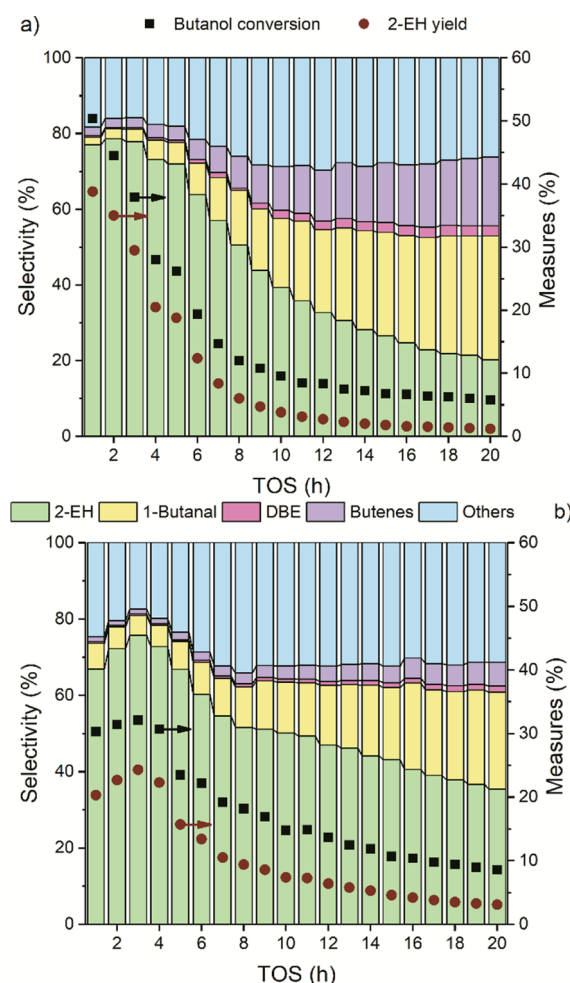

Figure 5. TOS dependences of BuOH conversion, 2-EH yield, and main product selectivities over Ca-HAP (a) and CaMg2.5-HAP (b). T = 573 K and LHSV = 0.11 $L \cdot L_{cat}^{-1} h^{-1}$.

CaMg2.5-HAP, there are predominantly acid sites. Acid sites are less inclined to deactivation by aldehyde condensation products than base sites, as it is shown in the work.[57] This can be the reason of a slower loss of the CaMg2.5-HAP catalytic activity with increasing TOS during the BuOH-to-2-EH process compared to Ca-HAP.

Table 5 shows the values of selectivities in the BuOH-to-2-EH process over HAP catalysts at BuOH conversion ~19%. The highest value of 2-EH selectivity of 62.0% is achieved in the presence of CaMg2.5-HAP. The sample CaSr5-HAP is less selective toward the target product (38.6%) and more selective for butene (9.5%).

Thus, the substitution of Ca^{2+} ions in the structure of Ca-HAP for Mg^{2+} or Sr^{2+} and the formation of the structure defects cause a certain change in the acid−base surface characteristics of HAPs, which determine the catalyst activity and selectivity for alcohol condensation products. Various localization of the substituted ions in the calcium positions of the HAP structure, that is, the atoms coordinating with nine oxygen atoms Ca(1) and seven oxygen atoms Ca(2), results in the formation of base sites of different strength: medium and weak ones, respectively. As the Mg^{2+} ion radius is smaller than the Ca^{2+} radius, the probability of substitution of the Ca(1) position by magnesium is higher. This leads to a decrease in basicity, namely the disappearance of strong base sites, and to

Table 5. Initial Product Selectivities in the BuOH-to-2-EH Process over the HAP Catalysts at T = 573 K

catalyst	LHSV, L·L$_{cat}^{-1}$ h^{-1}	conversion, %	selectivity, %				
			2-EH	1-butanal	DBE	butenes	others
Ca-HAP	0.17	18.4	55.0	9.0	0.8	6.2	29.1
CaMg2.5-HAP	0.17	19.8	62.0	11.5	0.6	2.7	23.2
CaMg5-HAP	0.11	18.9	49.6	10.1	1.6	4.1	34.6
CaSr5-HAP	0.08	18.5	38.6	10.8	1.5	9.5	39.5
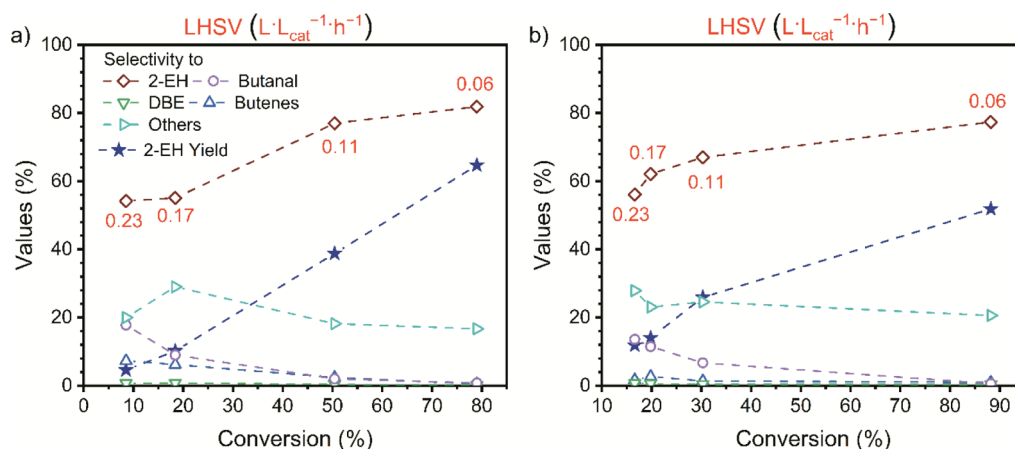
Figure 6. Dependence of product selectivity and yield on the conversion varied by changing the BuOH LHSV for Ca-HAP (a) and CaMg2.5-HAP (b). TOS = 1 h and T = 573 K.

an increase in LAS acidity due to the presence of Mg^{2+} cations on the surface.

The product distribution depending on BuOH conversion is obtained by varying the LHSV (Figure 6). It indicates that at 573 K the selectivity and yield of 2-EH gradually increase with the rising of BuOH conversion. At the same time, selectivity toward 1-butanal decreases. The selectivity for BuOH dehydration products, mainly butenes, is slightly dependent on the conversion. According to the received results, the key step of the BuOH-to-2-EH process at BuOH conversion up to 20% is the aldol condensation of 1-butanal, as 1-butanal is present in the products. At BuOH conversion of more than 30%, the key step of the process is the formation of 1-butanal, as often reported for the liquid-phase alcohol condensation.[58] For the HAP catalyst (a system that does not contain transition metals), the dehydrogenation of alcohols occurs over the base sites of the surface.[20]

In Figure S12, the temperature dependences of BuOH conversion, 2-EH yield, and selectivity for the main products over Ca-HAP and CaMg2.5-HAP catalysts are represented. With the increase of temperature from 573 to 673 K, the conversion of 1-butanol increases to 82.7% for Ca-HAP and 86.4% for CaMg2.5-HAP. 2-EH selectivity at a constant LHSV generally decreases with the rise of temperature, according to the thermodynamic process.[14] With the increase of the temperature in the presence of both catalysts, there is an increase in the selectivity for butenes and a decrease for 1-butanal. The DBE selectivity is 1−2% in the studied temperature range.

Overall, the best catalytic performance in the EtOH-to-BuOH and BuOH-to-2-EH processes is achieved in the presence of Ca-HAP and CaMg2.5-HAP catalysts. However, the highest selectivity of BuOH, C$_{4+}$ oxygenates, and 2-EH at the same alcohol conversion is reached over the Mg-containing catalyst. In addition, calcium substitution by 2.5 mol % of

magnesium in the structure of HAP provides the advanced resistance of the catalyst to deactivation with increasing TOS. In the process of EtOH condensation over CaMg2.5-HAP, selectivity values of 57% for BuOH and 79.2% for C$_{4+}$ oxygenates at 573 K and 0.36 L·L$_{cat}^{-1}$·h^{-1} are achieved. The yields of BuOH and C$_{4+}$ oxygenates reach values of 19.2 and 32.9% at a temperature of 598 K and LHSV = 0.12 L·L$_{cat}^{-1}$·h^{-1}. The BuOH yields achieved in the presence of Mg-containing HAP in the EtOH-to-BuOH process at temperatures of 573 and 598 K exceed all those for the known calcium[20−22] and strontium[26,27] HAPs (see Table S4). In the process of BuOH condensation over CaMg2.5-HAP, the highest value of 2-EH selectivity is 77.5% at 573 K and 0.11 L·L$_{cat}^{-1}$·h^{-1}, and the highest yield of 2-EH is 68.3% at 573 K and 0.06 L·L$_{cat}^{-1}$·h^{-1} (Table S5).

■ CONCLUSIONS

Catalysts modified with magnesium and strontium are prepared by partial substitution of Ca^{2+} ions in the crystal structure of HAP and characterized by XRD, SEM, EDX, XPS, FTIR, and NMR analyses and TPD of NH$_3$ and CO$_2$. It was found that partial replacement of Ca^{2+} ions by Mg^{2+} and Sr^{2+} in the structure of calcium-containing HAP causes the deformation of its crystal lattice with the possible formation of amorphous calcium phosphate species. It determines a decrease in the number and strength of the surface base sites of the catalysts and a redistribution of the strength of acid sites. In the case of CaMg2.5-HAP, a significant increase in the number of acid sites is observed.

Catalysts have been studied in the processes of vapor-phase condensation of EtOH to BuOH and BuOH to 2-EH; however, gradual deactivation of the catalysts occurs as a result of the blocking of aldol condensation sites. The highest selectivity values for BuOH and C$_{4+}$ oxygenates (57 and 79.2% at 573 K and 0.36 L·L$_{cat}^{-1}$·h^{-1}) and for 2-EH (77.5% at 573 K

and 0.11 $L \cdot L_{cat}^{-1} \cdot h^{-1}$) are achieved over CaMg2.5-HAP, which also showed an advanced resistance to deactivation with increasing TOS. Ca(Mg)-HAPs are shown to be promising catalysts for the sustainable production of industrially important higher linear and branched alcohols from biomass-derived alcohols.

■ ASSOCIATED CONTENT

Ⓢ Supporting Information

The Supporting Information is available free of charge at https://pubs.acs.org/doi/10.1021/acssuschemeng.1c06094.

> XRD patterns with designation of the HAP planes; SEM images; EDX distribution maps for the elements on the surface; XPS, ^{31}P MAS, and ^1H MAS NMR spectra; TPD-CO_2/NH_3 profiles of the HAP samples; ratio of Ca/P and (Ca + M)/P in the samples (M—Mg, Sr); ^1H–^{13}C CP/MAS and ^1H MAS NMR spectra of Ca-HAP after catalysis; TOS and temperature dependences of ethanol conversion and the dependences of product selectivity and yield on ethanol conversion over CaMg2.5-HAP; temperature dependences of 1-butanol conversion over Ca-HAP and CaMg2.5-HAP; and additional indices of ethanol and 1-butanol conversion over the studied HAP catalysts (PDF)

■ AUTHOR INFORMATION

Corresponding Author

Olga V. Larina − *L.V. Pisarzhevskii Institute of Physical Chemistry, The National Academy of Sciences of Ukraine, 03028 Kyiv, Ukraine;* ⓞ orcid.org/0000-0001-6359-1512; Email: olga.larina@ukr.net

Authors

Oksana V. Zikrata − *L.V. Pisarzhevskii Institute of Physical Chemistry, The National Academy of Sciences of Ukraine, 03028 Kyiv, Ukraine*

Karina V. Valihura − *L.V. Pisarzhevskii Institute of Physical Chemistry, The National Academy of Sciences of Ukraine, 03028 Kyiv, Ukraine*

Pavlo I. Kyriienko − *L.V. Pisarzhevskii Institute of Physical Chemistry, The National Academy of Sciences of Ukraine, 03028 Kyiv, Ukraine;* ⓞ orcid.org/0000-0003-1533-3492

Dmytro Yu. Balakin − *Institute of Physics, The National Academy of Sciences of Ukraine, 03028 Kyiv, Ukraine*

Ivan Khalakhan − *Department of Surface and Plasma Science, Faculty of Mathematics and Physics, Charles University, 18000 Prague, Czech Republic;* ⓞ orcid.org/0000-0003-2929-4148

Katerina Veltruská − *Department of Surface and Plasma Science, Faculty of Mathematics and Physics, Charles University, 18000 Prague, Czech Republic*

Andraž Krajnc − *Department of Inorganic Chemistry and Technology, National Institute of Chemistry, SI-1001 Ljubljana, Slovenia;* ⓞ orcid.org/0000-0003-2249-602X

Gregor Mali − *Department of Inorganic Chemistry and Technology, National Institute of Chemistry, SI-1001 Ljubljana, Slovenia;* ⓞ orcid.org/0000-0002-9012-2495

Sergiy O. Soloviev − *L.V. Pisarzhevskii Institute of Physical Chemistry, The National Academy of Sciences of Ukraine, 03028 Kyiv, Ukraine*

Svitlana M. Orlyk − *L.V. Pisarzhevskii Institute of Physical Chemistry, The National Academy of Sciences of Ukraine, 03028 Kyiv, Ukraine*

Complete contact information is available at:
https://pubs.acs.org/10.1021/acssuschemeng.1c06094

Author Contributions

O.V.Z.: preparation of the samples, performing particular experiments (catalytic tests and FTIR spectroscopic measurements), data collection and presentation, and writing of original draft. O.V.L.: management and coordination responsibility for research activity planning and execution, conceptualization of idea, performing experiments and data collection, writing of original draft, reviewing and editing of the manuscript, and presentation of the published work. K.V.V.: preparation of the samples, performing particular experiments and data collection, and reviewing and editing of the manuscript. P.I.K.: conceptualization of idea, performing particular experiments (XRD and FTIR spectroscopic measurements) and data collection, writing of original draft, and reviewing and editing of the manuscript. D.Y.B.: performing particular experiments (one-pass TPD measurements), application of computational and other formal techniques to analyze the obtained data, and processing and discussion of the data. I.K.: performing particular experiments (measurements by SEM and EDX spectroscopy), processing and discussion of obtained data, and reviewing and editing of the manuscript. K.V.: performing particular experiments (X-ray photoelectron spectroscopic measurements), processing and discussion of the obtained data, and reviewing and editing of the manuscript. A.K.: performing particular experiments (^1H MAS and ^1H–^{13}C CP/MAS NMR measurements) and processing and discussion of the obtained data. G.M.: performing particular experiments (^{31}P and ^1H MAS NMR measurements), application of computational and other formal techniques to analyze the obtained data, processing and discussion of the data, and reviewing and editing of the manuscript. S.O.S.: critical review and commentary, reviewing and editing of the manuscript, management and coordination responsibility for research activity planning, and acquisition of financial support for the project leading to this publication. S.M.O.: critical review and commentary, reviewing and editing of the manuscript, management and coordination responsibility for research activity planning, and acquisition of financial support for the project leading to this publication.

Notes

The authors declare no competing financial interest.

■ ACKNOWLEDGMENTS

■ REFERENCES

(1) Sun, J.; Wang, Y. Recent Advances in Catalytic Conversion of Ethanol to Chemicals. *ACS Catal.* **2014**, *4*, 1078−1090.

(2) Pang, J.; Zheng, M.; Zhang, T. Synthesis of Ethanol and Its Catalytic Conversion. *Advances in Catalysis*; Elsevier Inc., 2019; Vol. *64*, pp 89−191.

(3) Dagle, R. A.; Winkelman, A. D.; Ramasamy, K. K.; Lebarbier Dagle, V.; Weber, R. S. Ethanol as a renewable building block for fuels and chemicals. *Ind. Eng. Chem. Res.* **2020**, *59*, 4843−4853.

(4) Pomalaza, G.; Arango Ponton, P.; Capron, M.; Dumeignil, F. Ethanol-to-butadiene: The reaction and its catalysts. *Catal. Sci. Technol.* **2020**, *10*, 4860−4911.

(5) Kyriienko, P. I.; Larina, O. V.; Soloviev, S. O.; Orlyk, S. M. Catalytic Conversion of Ethanol Into 1,3-Butadiene: Achievements and Prospects: A Review. *Theor. Exp. Chem.* **2020**, *56*, 213−242.

(6) Posada, J. A.; Patel, A. D.; Roes, A.; Blok, K.; Faaij, A. P. C.; Patel, M. K. Potential of bioethanol as a chemical building block for biorefineries: preliminary sustainability assessment of 12 bioethanol-based products. *Bioresour. Technol.* **2013**, *135*, 490−499.

(7) Mohsenzadeh, A.; Zamani, A.; Taherzadeh, M. J. Bioethylene Production from Ethanol: A Review and Techno-economical Evaluation. *ChemBioEng Rev.* **2017**, *4*, 75−91.

(8) Eagan, N. M.; Kumbhalkar, M. D.; Buchanan, J. S.; Dumesic, J. A.; Huber, G. W. Chemistries and processes for the conversion of ethanol into middle-distillate fuels. *Nat. Rev. Chem.* **2019**, *3*, 223−249.

(9) Petersen, A. M.; Chireshe, F.; Okoro, O.; Gorgens, J.; Van Dyk, J. Evaluating refinery configurations for deriving sustainable aviation fuel from ethanol or syncrude. *Fuel Process. Technol.* **2021**, *219*, 106879.

(10) Knothe, G. Synthesis, applications, and characterization of Guerbet compounds and their derivatives. *Lipid Technol.* **2002**, *September*, 101−104.

(11) Bahrmann, H.; Hahn, H.-D.; Mayer, D.; Frey, G. D. 2-Ethylhexanol https://onlinelibrary.wiley.com/doi/10.1002/14356007.a10_137.pub3 (accessed Jan 15, 2013).

(12) Wu, L.; Moteki, T.; Gokhale, A. A.; Flaherty, D. W.; Toste, F. D. Production of Fuels and Chemicals from Biomass: Condensation Reactions and Beyond. *Chem* **2016**, *1*, 32−58.

(13) Thach, S.; Shong, R.; Dwarakanath, V.; Winslow, G. Method of Manufacture of Guerbet Alcohols For Making Surfactants Used In Petroleum Industry Operations. U.S. Patent 20,130,068,457 A1, 2013.

(14) Gabriëls, D.; Hernández, W. Y.; Sels, B.; Van Der Voort, P.; Verberckmoes, A. Review of catalytic systems and thermodynamics for the Guerbet condensation reaction and challenges for biomass valorization. *Catal. Sci. Technol.* **2015**, *5*, 3876−3902.

(15) Patel, A. D.; Telalović, S.; Bitter, J. H.; Worrell, E.; Patel, M. K. Analysis of sustainability metrics and application to the catalytic production of higher alcohols from ethanol. *Catal. Today* **2015**, *239*, 56−79.

(16) Larina, O. V.; Valihura, K. V.; Kyriienko, P. I.; Vlasenko, N. V.; Balakin, D. Y.; Khalakhan, I.; Čendak, T.; Soloviev, S. O.; Orlyk, S. M. Successive vapour phase Guerbet condensation of ethanol and 1-butanol over Mg-Al oxide catalysts in a flow reactor. *Appl. Catal., A* **2019**, *588*, 117265.

(17) Valihura, K. V.; Larina, O. V.; Kyriienko, P. I.; Vlasenko, N. V.; Soloviev, S. O. Effect of composition of Mg-Al-oxide systems on their catalytic properties in the production of 2-ethyl-1-hexanol in vapor-phase condensation of 1-butanol in a flow system. *Theor. Exp. Chem.* **2019**, *55*, 337−344.

(18) Eagan, N. M.; Moore, B. M.; McClelland, D. J.; Wittrig, A. M.; Canales, E.; Lanci, M. P.; Huber, G. W.; McCelland, D. J.; Wittrig, A. M.; Canales, E.; et al. Catalytic synthesis of distillate-range ethers and olefins from ethanol through Guerbet coupling and etherification. *Green Chem.* **2019**, *21*, 3300−3318.

(19) Kozlowski, J. T.; Davis, R. J. Heterogeneous Catalysts for the Guerbet Coupling of Alcohols. *ACS Catal.* **2013**, *3*, 1588−1600.

(20) Pinzón, M.; Cortés-Reyes, M.; Herrera, C.; Larrubia, M. Á.; Alemany, L. J. Ca-based bifunctional acid-basic model-catalysts for n-

butanol production from ethanol condensation. *Biofuels, Bioprod. Biorefin.* **2021**, *15*, 218−230.

(21) Fihri, A.; Len, C.; Varma, R. S.; Solhy, A. Hydroxyapatite: A review of syntheses, structure and applications in heterogeneous catalysis. *Coord. Chem. Rev.* **2017**, *347*, 48−76.

(22) Tsuchida, T.; Sakuma, S.; Takeguchi, T.; Ueda, W. Direct Synthesis of n-Butanol from Ethanol over Nonstoichiometric Hydroxyapatite. *Ind. Eng. Chem. Res.* **2006**, *45*, 8634−8642.

(23) Tsuchida, T.; Kubo, J.; Yoshioka, T.; Sakuma, S.; Takeguchi, T.; Ueda, W. Reaction of ethanol over hydroxyapatite affected by Ca/P ratio of catalyst. *J. Catal.* **2008**, *259*, 183−189.

(24) Wang, Q.-N.; Zhou, B.-C.; Weng, X.-F.; Lv, S.-P.; Schüth, F.; Lu, A.-H. Hydroxyapatite nanowires rich in [Ca-O-P] sites for ethanol direct coupling showing high C6-12 alcohol yield. *Chem. Commun.* **2019**, *55*, 10420−10423.

(25) Hanspal, S.; Young, Z. D.; Prillaman, J. T.; Davis, R. J. Influence of surface acid and base sites on the Guerbet coupling of ethanol to butanol over metal phosphate catalysts. *J. Catal.* **2017**, *352*, 182−190.

(26) Ogo, S.; Onda, A.; Yanagisawa, K. Selective synthesis of 1-butanol from ethanol over strontium phosphate hydroxyapatite catalysts. *Appl. Catal., A* **2011**, *402*, 188−195.

(27) Ogo, S.; Onda, A.; Iwasa, Y.; Hara, K.; Fukuoka, A.; Yanagisawa, K. 1-Butanol synthesis from ethanol over strontium phosphate hydroxyapatite catalysts with various Sr/P ratios. *J. Catal.* **2012**, *296*, 24−30.

(28) Silvester, L.; Lamonier, J.-F.; Lamonier, C.; Capron, M.; Vannier, R.-N.; Mamede, A.-S.; Dumeignil, F. Guerbet Reaction over Strontium-Substituted Hydroxyapatite Catalysts Prepared at Various (Ca+Sr)/P Ratios. *ChemCatChem* **2017**, *9*, 2250−2261.

(29) Han, X.; An, H.; Zhao, X.; Wang, Y. Influence of acid-base properties on the catalytic performance of Ni/hydroxyapatite in n-butanol Guerbet condensation. *Catal. Commun.* **2020**, *146*, 106130.

(30) Wang, J.; Yang, W.; Wu, C.; Gong, Y.; Zhang, J.; Shen, C. Upgrading n-Butanol to Branched Alcohols over Ni/CaxMgyO. *ACS Sustainable Chem. Eng.* **2020**, *8*, 16960−16967.

(31) Jordison, T. L.; Peereboom, L.; Miller, D. J. Impact of Water on Condensed Phase Ethanol Guerbet Reactions. *Ind. Eng. Chem. Res.* **2016**, *55*, 6579−6585.

(32) Valihura, K. V.; Larina, O. V.; Kyriienko, P. I.; Balakin, D. Y.; Soloviev, S. O. Influence of Modifying Additives of Lanthanum and Cerium Oxides on Acid−Base Characteristics and Catalytic Properties of MgO-Al2O3 Systems in the Process of Gas-Phase Conversion of Ethanol to 1-Butanol. *Theor. Exp. Chem.* **2021**, *56*, 404−411.

(33) Cimino, S.; Apuzzo, J.; Lisi, L. MgO Dispersed on Activated Carbon as Water Tolerant Catalyst for the Conversion of Ethanol into Butanol. *Appl. Sci.* **2019**, *9*, 1371.

(34) Larina, O. V.; Kyriienko, P. I.; Shcherban, N. D.; Yaremov, P. S.; Balakin, D. Y.; Khalakhan, I.; Veltruská, K.; Soloviev, S. O.; Orlyk, S. M. Carbon-Supported Mg−Al Oxide Hybrid Catalysts for Aqueous Ethanol Conversion into 1-Butanol in a Flow Reactor. *Ind. Eng. Chem. Res.* **2021**, *60*, 11964−11976.

(35) Scofield SFs—Al X-ray—Theoretical Calculation—Central Field Potential. https://xpslibrary.com/sf-table-scofield-theoretical/ (accessed Aug 25, 2021).

(36) O'Donnell, M. D.; Fredholm, Y.; de Rouffignac, A.; Hill, R. G. Structural analysis of a series of strontium-substituted apatites. *Acta Biomater.* **2008**, *4*, 1455−1464.

(37) Yasukawa, A.; Ouchi, S.; Kandori, K.; Ishikawa, T. Preparation and characterization of magnesium-calcium hydroxyapatites. *J. Mater. Chem.* **1996**, *6*, 1401−1405.

(38) Othmani, M.; Aissa, A.; Grelard, A.; Das, R. K.; Oda, R.; Debbabi, M. Synthesis and characterization of hydroxyapatite-based nanocomposites by the functionalization of hydroxyapatite nanoparticles with phosphonic acids. *Colloids Surf., A* **2016**, *508*, 336−344.

(39) Edwin, N.; Saranya, S.; Wilson, P. Strontium incorporated hydroxyapatite/hydrothermally reduced graphene oxide nanocomposite as a cytocompatible material. *Ceram. Int.* **2019**, *45*, 5475−5485.

(40) Sønju Clasen, A. B.; Ruyter, I. E. Quantitative determination of type A and type B carbonate in human deciduous and permanent

enamel by means of Fourier transform infrared spectrometry. *Adv. Dent. Res.* **1997**, *11*, 523−527.

(41) Gadaleta, S. J.; Paschalis, E. P.; Betts, F.; Mendelsohn, R.; Boskey, A. L. Fourier transform infrared spectroscopy of the solution-mediated conversion of amorphous calcium phosphate to hydroxyapatite: new correlations between X-ray diffraction and infrared data. *Calcif. Tissue Int.* **1996**, *58*, 9−16.

(42) Silvester, L.; Lamonier, J.-F.; Vannier, R.-N.; Lamonier, C.; Capron, M.; Mamede, A.-S.; Pourpoint, F.; Gervasini, A.; Dumeignil, F.; Lamonier, C.; Capron, M.; Mamede, A.-S.; Pourpoint, F.; et al. Structural, textural and acid-base properties of carbonates-containing hydroxyapatites. *J. Mater. Chem. C* **2014**, *2*, 11073−11090.

(43) Ben Osman, M.; Diallo-Garcia, S.; Herledan, V.; Brouri, D.; Yoshioka, T.; Kubo, J.; Millot, Y.; Costentin, G. Discrimination of Surface and Bulk Structure of Crystalline Hydroxyapatite Nanoparticles by NMR. *J. Phys. Chem. C* **2015**, *119*, 23008−23020.

(44) Tseng, Y.-H.; Mou, C.-Y.; Chan, J. C. C. Solid-state NMR study of the transformation of octacalcium phosphate to hydroxyapatite: A mechanistic model for central dark line formation. *J. Am. Chem. Soc.* **2006**, *128*, 6909−6918.

(45) Kolmas, J.; Kolodziejski, W. Inverse 31P → 1H NMR cross-polarization in hydrated nanocrystalline calcium hydroxyapatite. *Chem. Phys. Lett.* **2012**, *554*, 128−132.

(46) Mathew, R.; Gunawidjaja, P. N.; Izquierdo-Barba, I.; Jansson, K.; García, A.; Arcos, D.; Vallet-Regí, M.; Edén, M. Solid-state 31P and 1H NMR investigations of amorphous and crystalline calcium phosphates grown biomimetically from a mesoporous bioactive glass. *J. Phys. Chem. C* **2011**, *115*, 20572−20582.

(47) Osman, M. B.; Krafft, J. M.; Thomas, C.; Yoshioka, T.; Kubo, J.; Costentin, G. Importance of the Nature of the Active Acid/Base Pairs of Hydroxyapatite Involved in the Catalytic Transformation of Ethanol to n-Butanol Revealed by Operando DRIFTS. *ChemCatChem* **2019**, *11*, 1765−1778.

(48) Di Cosimo, J. I.; Apesteguía, C. R.; Ginés, M. J. L.; Iglesia, E. Structural Requirements and Reaction Pathways in Condensation Reactions of Alcohols on MgyAlOx Catalysts. *J. Catal.* **2000**, *190*, 261−275.

(49) Young, Z. D.; Hanspal, S.; Davis, R. J. Aldol Condensation of Acetaldehyde over Titania, Hydroxyapatite, and Magnesia. *ACS Catal.* **2016**, *6*, 3193−3202.

(50) Shen, W.; Tompsett, G. A.; Xing, R.; Curtis Conner, W.; Huber, G. W.; Curtis Conner, W.; Huber, G. W. Vapor phase butanal self-condensation over unsupported and supported alkaline earth metal oxides. *J. Catal.* **2012**, *286*, 248−259.

(51) Rekoske, J. E.; Barteau, M. A. Kinetics, selectivity, and deactivation in the aldol condensation of acetaldehyde on anatase titanium dioxide. *Ind. Eng. Chem. Res.* **2011**, *50*, 41−51.

(52) Larina, O. V.; Remezovskyi, I. M.; Kyriienko, P. I.; Soloviev, S. O.; Orlyk, S. M. 1,3-Butadiene production from ethanol−water mixtures over Zn−La−Zr−Si oxide catalyst. *React. Kinet., Mech. Catal.* **2019**, *127*, 903−915.

(53) Cabello González, G. M.; Concepción, P.; Villanueva Perales, A. L.; Martínez, A.; Campoy, M.; Vidal-Barrero, F. Ethanol conversion into 1,3-butadiene over a mixed Hf-Zn catalyst: Effect of reaction conditions and water content in ethanol. *Fuel Process. Technol.* **2019**, *193*, 263−272.
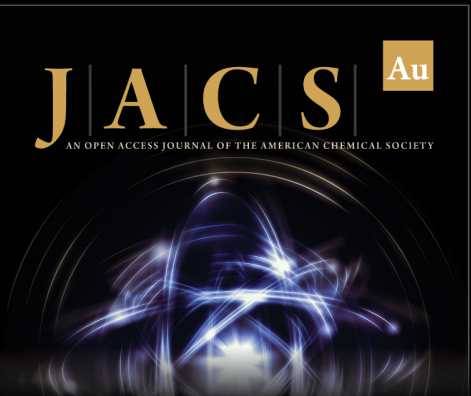
(54) Scalbert, J.; Thibault-Starzyk, F.; Jacquot, R.; Morvan, D.; Meunier, F. Ethanol condensation to butanol at high temperatures over a basic heterogeneous catalyst: How relevant is acetaldehyde self-aldolization? *J. Catal.* **2014**, *311*, 28−32.

(55) Angelici, C.; Weckhuysen, B. M.; Bruijnincx, P. C. A. Chemocatalytic conversion of ethanol into butadiene and other bulk chemicals. *ChemSusChem* **2013**, *6*, 1595−1614.

(56) Ho, C. R.; Shylesh, S.; Bell, A. T. Mechanism and Kinetics of Ethanol Coupling to Butanol over Hydroxyapatite. *ACS Catal.* **2016**, *6*, 939−948.

(57) Ordomsky, V. V.; Sushkevich, V. L.; Ivanova, I. I. Study of acetaldehyde condensation chemistry over magnesia and zirconia supported on silica. *J. Mol. Catal. A: Chem.* **2010**, *333*, 85−93.

(58) Benito, P.; Vaccari, A.; Antonetti, C.; Licursi, D.; Schiarioli, N.; Rodriguez-Castellón, E.; Raspolli Galletti, A. M. Tunable copper-hydrotalcite derived mixed oxides for sustainable ethanol condensation to n-butanol in liquid phase. *J. Cleaner Prod.* **2019**, *209*, 1614−1623.